INORGANIC CHEMISTRY FRONTIERS

RESEARCH ARTICLE

View Article Online
View Journal

Cite this: DOI: 10.1039/d5qi00709g

Boosting the growth kinetics of extra-large-pore zeolite ZEO-1†

Haijun Yu, ‡[a,b] Wenjing Zhang,‡[a] Yiqing Sun,[b] Guangying Fu,[b] Doudou Cai,[b] Nourrdine Chaouati,[c] Ludovic Pinard,[c] Mohammad Fahda,[c] Feng Shao, *[a] Peng Lu*[b] and Valentin Valtchev *[b,c]

ZEO-1, the first stable aluminosilicate zeolite with extra-large pores, marks a great breakthrough in the zeolite community after decades of exploration and endeavors, opening possibilities for processing bulky substrates. However, the long synthesis cycle and relatively low reproducibility hinder the wide application of this intriguing material. This work developed a 'deficient fluoride approach' for ZEO-1 zeolite synthesis by adding a small amount of fluoride to induce a charge imbalance between the OSDA and fluoride. This approach significantly accelerates crystallization (15 times faster than the reported method) and achieves higher reproducibility than the originally reported protocol. Crystallization kinetics studies demonstrate the accelerating effect of stoichiometrically deficient fluoride anions on the nucleation and crystallization process. The ZEO-1 zeolites synthesized *via* the 'deficient fluoride approach' show catalytic activity for phenol alkylation with *tert*-butyl alcohol comparable to that of ZEO-1_{LCS}, but the products are evenly distributed, suggesting that more Brønsted acid sites might have been successfully introduced in the 16 MR channels. This work provides an incentive for feasible academic study and application of ZEO-1.

Received 11th March 2025,
Accepted 15th May 2025

DOI: 10.1039/d5qi00709g

rsc.li/frontiers-inorganic

Introduction

Zeolites, as a class of inorganic microporous materials, are constructed from TO_4 tetrahedra (T = Si, Al, P, Ge, Ga, *etc.*) that form regular pore structures through shared vertices at the molecular scale. The adjustable pore size and aperture, as well as the diversity of framework composition, make zeolites one of the most successful materials widely implemented in the petrochemical and fine chemical industries as adsorbents, membranes, and catalysts.[1–4] The intrinsic micropores in zeolites endow them with shape selectivity to screen molecules based on size differences; however, these micropores also act as barriers in applications involving bulky molecules. Hence, the quest for zeolites with extra-large pores, which are delimited by rings of more than 12 members (*i.e.*, greater than 12-membered rings), has become a "holy grail" in zeolite research.

In 1988, Davis *et al.*[5] synthesized the first extra-large pore size 18 MR aluminum phosphate zeolite VPI-5, marking the successful beginning of extra-large microporous zeolite synthesis. The emergence of extra-large pore size zeolites has bridged the gap between microporous zeolites and amorphous mesoporous molecular sieves, pushing zeolite research into a new era. Subsequently, more extra-large pore size zeolites were synthesized, leading to progress in catalytic research involving bulky molecules. In 1991, Estermann *et al.*[6] reported the first 3D extra-large pore size aluminum phosphate zeolite with 20 MR (–CLO). In addition, Corma's research group[7–14] reported a series of 3D extra-large-pore germanosilicate zeolites (ITQ series) during the past decade; however, the incorporation of Ge into the framework significantly compromises their thermal and hydrothermal stability due to Ge hydrolysis under humid conditions. A great breakthrough in extra-large-pore zeolite synthesis was recently achieved by Camblor, Chen and co-workers,[15] who reported the successful synthesis of an aluminosilicate zeolite, named ZEO-1 (IZA code: **JZO**), using a bulky phosphorus-containing organic mono-cation as the organic structure directing agent (OSDA). ZEO-1 has a 3D interconnected channel system composed of extra-large 16-ring and 12-ring pores with a fully-connected framework, exhibiting adsorption capacity superior to that of the conventional ultra-stable Y (USY) zeolite for large-sized dye molecules.

[a]*Key Laboratory of Marine Chemistry Theory and Technology, Ministry of Education, College of Chemistry and Chemical Engineering, Ocean University of China, Qingdao 266100, China. E-mail: feng.shao@ouc.edu.cn*

[b]*The ZeoMat Group, Key Laboratory of Photoelectric Conversion and Utilization of Solar Energy, Qingdao New Energy Shandong Laboratory, Qingdao Institute of Bioenergy and Bioprocess Technology, Chinese Academy of Science, Laoshan District, CN-266101 Qingdao, China. E-mail: valentin.valtchev@ensicaen.fr, lupeng@qibebt.ac.cn*

[c]*Normandie University, ENSICAEN, UNICAEN, CNRS, Laboratoire Catalyse et Spectrochimie, F-14000 Caen, France*

†Electronic supplementary information (ESI) available. See DOI: https://doi.org/10.1039/d5qi00709g

‡These authors contributed equally to this work.

ZEO-1 containing phosphorus shows a lower conversion rate and higher selectivity towards gasoline and diesel in heavy oil cracking compared to commonly used commercial zeolite catalysts such as USY, MFI, and Beta. Although ZEO-1 exhibits a novel topological structure with excellent adsorption and catalytic properties, its practical industrial application is hindered by synthesis challenges. The sluggish nucleation process prolongs the synthesis duration, while extended hydrothermal treatment promotes the formation of an undesirable dense quartz phase, collectively resulting in a long synthesis cycle and low experimental repeatability. To address the long synthesis cycle, ZEO-1 was successfully obtained with a shortened crystallization time (8 days)[16] by substituting sodium aluminate and silica sol as alternative Al and Si sources together with a lower fluoride content in the synthesis, which, however, still needs improvement considering practical production and energy consumption. In addition, zeolite synthesis reproducibility is a well-known conundrum within the zeolite community, where developing a consistent recipe that works in every laboratory is challenging. Thus, developing feasible synthesis strategies for shortening the production cycle and boosting the reproducibility of ZEO-1 zeolites is crucial for both academic study and practical application.

In this work, we demonstrate the successful synthesis of ZEO-1 zeolites with a significantly improved crystallization rate and high reproducibility using a tentatively termed "deficient fluoride approach", wherein fluoride anions from two different fluoride sources were used to achieve a charge imbalance between the fluoride anions and organic cations in the synthetic gel, *i.e.*, providing fewer fluoride anions than required to stoichiometrically balance the charge of the OSDA. Synthesis parameters, *e.g.*, gel molar compositions and crystallization temperatures, were thoroughly investigated to probe the optimized synthesis window for ZEO-1 zeolites. The physicochemical properties of ZEO-1 zeolites in different forms, as-made, calcined, and calcined & NH_4Cl-washed, were unveiled using comprehensive characterization techniques, including PXRD, SEM, TEM, solid-state NMR, NH_3-TPD, Py-FTIR, *etc*. The crystallization kinetics of ZEO-1 zeolites was investigated by analyzing the products obtained at different heating times using spectroscopy techniques. The role of fluoride addition in the crystallization of ZEO-1 zeolites was tentatively discussed. Finally, the catalytic performance of ZEO-1 zeolites in the alkylation of phenol with *tert*-butanol was evaluated in comparison with commercial USY and Beta zeolites.

Experimental

OSDA synthesis

The OSDA used in this work is the tricyclohexylmethylphosphonium cation (TCyMP, Fig. S1†), which was synthesized according to a previously reported method.[15] In a typical synthesis procedure, 28.62 g (0.10 mol) of tricyclohexylphosphine (Energy Chemical, 98%) was added to a round-bottom flask containing 250 mL of acetonitrile (Sinopharm Chemical Reagent, AR) under magnetic stirring in an ice bath. Subsequently, 49.93 g (0.35 mol, 3.50 eq.) of iodomethane (MeI, Energy Chemical, 99.5%) was added dropwise *via* an addition funnel. The mixture was allowed to react for 48 hours at room temperature, and then acetonitrile and iodomethane were removed using a rotavapor under vacuum to obtain tricyclohexylmethylphosphonium iodide (yield: *ca.* 98%).

In batch mode, the iodide salt was exchanged to its hydroxide form using an anion exchange resin (Xidian, 1.1 mequiv./1 mL). The exchanged solution was concentrated using rotary evaporation under vacuum, and the final solution concentration was determined by titration with 0.1 N HCl (Beijing North Weiye Institute of Measuring and Testing Technology), using phenolphthalein as an indicator.

Zeolite synthesis

The synthesis of ZEO-1 zeolites was carried out in hydroxide medium according to previously reported procedures.[15] For syntheses involving the addition of fluoride anions, two fluoride sources, hydrofluoric acid (HF) and ammonium fluoride (NH_4F), were used.

In a typical synthesis using HF, 9.473 g (3.75 mmol) of the organic structure directing agent (SDAOH) was added to a 50 mL plastic beaker, followed by 0.125 g (0.3 mmol) of aluminum isopropyl alcohol ($Al(O\text{-}iPr)_3$, Shanghai Mcklin, AR). After stirring at 200 rpm for 2 h, 3.125 g (1.5 mmol) of tetraethyl orthosilicate (TEOS, Sinopharm Chemical Reagent, 28.4 wt% SiO_2) was added to the solution, and the mixture was hydrolyzed overnight at room temperature. The resulting clear sol was aged in an oven at 100 °C for 6 h to remove excess water and ethanol. In a fume hood, 0.13 mL (3.0 mmol) of HF (Merck, 48%) was carefully added using a pipette, and the mixture was manually homogenized for 15 min to obtain a viscous gel or dry powdery gel with a final molar composition of 1.0 SiO_2 : 0.5 SDAOH : 0.02 Al_2O_3 : x HF : 10 H_2O, where x = 0.05–0.7. Then, the gel was transferred into a Teflon-lined autoclave, placed in a convection oven, and heated at 175 °C and 190 °C for varying durations. After cooling down to room temperature, the product was centrifuged at 12 000 rpm and washed with 40 mL deionized water, 40 mL ethanol and 20 mL acetone. The wet powdery product was dried for 2 h in a convection oven at 100 °C to obtain the as-made product. The as-made product was calcined in a muffle furnace in air using a reported procedure.[16] The calcination procedure was as follows: the sample was heated from room temperature to 150 °C for 45 min and then kept at 150 °C for 60 min to ensure that the water in the zeolite and the adsorbed gas were removed; subsequently, the temperature was increased to 600 °C over a 225 min ramp, and then kept at 600 °C for 6 h to eliminate OSDAs.

In a typical synthesis using NH_4F, 9.473 g (3.75 mmol) of the organic structure directing agent (SDAOH) was added to a 50 mL plastic beaker, followed by 0.125 g (0.3 mmol) of aluminum isopropyl alcohol ($Al(O\text{-}iPr)_3$). After stirring for 2 h, 3.125 g (1.5 mmol) of tetraethyl orthosilicate (TEOS) was added into the solution, and the mixture was hydrolyzed over-

night at room temperature. The clear sol obtained was aged in an oven at 100 °C for 6 h to remove excessive water and ethanol. In a fume hood, 0.25 mL (3.0 mmol) of NH_4F (Shanghai Aladdin, 40 wt%) solution was added carefully using a pipette, then manually homogenized for 15 min to obtain a viscous or dry powdery gel with a final molar composition of 1.0 SiO_2 : 0.5 SDAOH : 0.02 Al_2O_3 : x NH_4F : 10 H_2O, where x = 0.1–0.7. Furthermore, the gel was transferred into a Teflon-lined autoclave, placed in a convection oven, and heated at 190 °C for varying durations.

Removal of phosphorous species

Typically, 0.2 g of the calcined ZEO-1 zeolite was transferred into 25 mL sealed glass bottles, and 20 mL of a 0.5 M ammonium chloride solution was added. Subsequently, the glass bottles were placed in an oil bath at 60 °C and stirred at 300 rpm for 3 h to perform ion exchange. Then, the treated product was collected by centrifugation at 12 000 rpm for 10 min and washed with several times DI water until the pH was close to neutral. This process was repeated three times, and then the sample was dried overnight in an oven at 100 °C.

Characterization studies

Powder X-ray diffraction (XRD) patterns were collected using a Rigaku LabView diffractometer in the 2-theta range of 2 to 50° with 0.01° scan steps in theta–theta geometry under Cu Kα radiation. Thermogravimetric and differential thermal analysis (TG/DTA) was carried out using a Rigaku TG-DTA8122 thermal analyzer system in an air flow of 50 mL min^{-1}, with a heating rate of 10 °C min^{-1} from 30 to 1000 °C. Si, Al, and P contents were determined by inductively coupled plasma-optical emission spectrometry (ICP-OES) using a PerkinElmer NexION 350X. CHN elemental analysis was performed on a LECO CHNS-932 analyzer to determine the OSDA content. Scanning electron microscopy (SEM) was performed on a Hitachi S-4800 microscope with a cold field emission gun at 2 kV. High-resolution transmission electron microscopy (HRTEM) images were obtained using a JEOL-3200FS field-emission transmission electron microscope with an accelerating voltage of 300 kV and captured using a Gatan OneView CMOS camera. Argon and nitrogen physisorption isotherms were measured on a Quantachrome Autosorb iQ. Before the measurements, the samples were degassed at 300 °C under vacuum for 10 h. Temperature-programmed desorption of ammonia (NH_3-TPD) was carried out in a flow system equipped with a thermal conductivity detector (TCD). Using pyridine as a probe molecule, Fourier transform infrared spectra (FTIR) were collected on a Brucker Vertex 70 V spectrometer at a spectral resolution of 4 cm^{-1}. In a home-made vacuum infrared cell with CaF_2 windows, a self-supported wafer of the sample (about 10 mg cm^{-2}) was initially dried under vacuum at 450 °C for 2 h and then cooled down to 25 °C. A reference spectrum was recorded. Afterward, the wafer was saturated with pyridine vapor at 25 °C for 10 min and then evacuated again for 30 min to remove pyridine in the gas phase. Finally, the evacuated sample containing chemisorbed pyridine was subjected to temperature-programmed desorption from 30–450 °C, holding for 30 min at each temperature with a heating rate of 10 °C min^{-1}. FTIR spectra were recorded after cooling down to 25 °C. ^1H and ^{13}C liquid NMR spectra of the OSDA chloride in $CDCl_3$ solution were collected on a Bruker Avance III 400 spectrometer. Solid-state ^{29}Si, ^{27}Al, ^{31}P, and ^{19}F MAS NMR experiments were performed on a Bruker AVANCE III 400 spectrometer using a 4 mm triple resonance probe with a sample spinning rate of 14 kHz, operating at resonance frequencies of 156.4, 119.2, 161.9, 470.59 MHz, respectively. ^{29}Si MAS NMR spectra with high-power proton decoupling were recorded with a spinning rate of 10 kHz, a π/4 pulse length of 2.9 μs, and a recycle delay of 20 s. ^{27}Al MAS NMR spectra were recorded using a small-flip angle technique with a pulse length of 0.5 μs (<π/12), a recycle delay of 1 s, and a spinning rate of 14 kHz. Single-pulse ^{31}P MAS NMR experiments with ^1H decoupling were performed with a 90° pulse width of 4.9 μs, a recycle delay of 60 s, and a ^1H decoupling strength of 60 kHz. ^{19}F MAS NMR spectra were collected with a spinning rate of 14 000 kHz, a pulse width of 3.7 μs, and a relaxation delay of 5 s. The chemical shifts of ^{27}Al, ^{29}Si, and ^{31}P MAS NMR were externally referenced to 1 mol L^{-1} aqueous $Al(NO_3)_3$, TMS, and 85% H_3PO_4, respectively. $^{29}Si \times \{^1H\}$ cross-polarization (CP) MAS NMR spectra were obtained with a contact time of 5 ms (^1H frequency: 400.13 Hz).

The crystallization kinetics was analyzed using the Johnson–Mehl–Avrami–Kolmogorov (JMAK) model to calculate the rate constants at different temperatures:

$$x(t) = 1 - \exp(-kt^n)$$

In the JMAK model, $x(t)$ represents the crystallized fraction at time t, k denotes the temperature-dependent rate constant, and n is the Avrami exponent indicating the nucleation/growth dimensionality.

The activation energy was determined *via* the Arrhenius equation:

$$k = k_0 \exp(-E_a/RT)$$

where E_a represents the activation energy, T is the thermodynamic temperature, R is the gas constant (8.314 J mol^{-1} K^{-1}) and k_0 is the pre-exponential factor.

Phenol alkylation with *tert*-butanol

Phenol alkylation with *tert*-butyl alcohol was carried out in a batch reactor as follows: 200 mg of the zeolite catalyst, 565 mg (0.006 mol) of phenol, and 445 mg (0.006 mol) of *tert*-butanol were accurately weighed and combined in a 50 mL round-bottom flask. Additionally, 769 mg (0.006 mol) of nonane was added as an internal standard for chromatographic analysis. Finally, the mixture was homogenised with 19 mL of heptane. After cooling the mixture, the liquid phase was recovered using a syringe equipped with a filter to separate it from the solid catalyst. The distribution of the products was determined by analyzing the supernatant using a SCION gas chromatograph equipped with a 5 MS column (30 m length, 0.25 mm diameter, and 0.2 μm thickness). Phenol conversion and product

selectivity were estimated using the following equations:

$$\text{Phenol conv.} = \frac{\sum A(\text{aromatic products})}{\sum A(\text{aromatic products}) + A(\text{phenol})} \times 100$$

$$\text{Selectivity} = \frac{A(\text{product})}{\sum A(\text{aromatic products})} \times 100$$

Here, Phenol conv. denotes phenol conversion and A is the surface area of the corresponding chromatographic peak.

Catalytic tests were repeated three times using the USY zeolite as the reference catalyst. The standard deviations for product selectivity were ±3.5% for *ortho-tert*-butylphenol (*o*-TBP), ±2.6% for *para-tert*-butylphenol (*p*-TBP), and ±1.5% for 2,4-di-*tert*-butylphenol. The standard deviation for conversion was ±2.0%.

Results and discussion

Zeolite synthesis

The synthesis of ZEO-1 zeolites was initially investigated using HF as the fluoride source by systematically varying the F/SiO_2 and H_2O/SiO_2 ratios in the synthetic gel. The synthesis results are summarized in Table 1. At the typical synthesis temperature of 190 °C for ZEO-1 zeolites, upon increasing the F/SiO_2 ratio from 0 to 0.7 while keeping the H_2O/SiO_2 ratio constant at 10, the crystallization rate increased and then decreased. At a F/SiO_2 ratio of 0.2, well-crystallized ZEO-1 zeolites were obtained within 2 days (Table 1, entry 9), almost 8 times faster than the 15 days reported in the literature.[15] In contrast, only an amorphous phase was obtained at an F/SiO_2 ratio of 0.7, even after 9 days of heating (Table 1, entries 18 and 19). These observations indicate a critical fluoride concentration threshold beyond which zeolite crystallization is inhibited. Excess fluoride forms stable complexes with silicate species at high fluoride concentrations, preventing them from properly rearranging into lattice structures. The critical concentrations for the HF and NH_4F systems are 0.5 and 0.3, respectively, reflecting their differing acidities: the stronger acidity of HF enhances the stabilization of zeolite precursors, allowing higher fluoride tolerance. Furthermore, the effect of water content on the crystallization rate and crystallinity of ZEO-1 zeolites was also investigated. At a F/SiO_2 ratio of 0.2, reducing the H_2O/SiO_2 ratio to 5 significantly improved the crystallization rate, with well-crystallized ZEO-1 zeolites formed within 1 day (Table 1, entry 11). In contrast, a lower water content prolonged the crystallization time for the composition with a F/

Table 1 Summary of synthesis results using HF at 175 °C and 190 °C

Entry	F/SiO_2	H_2O/SiO_2	Time (day)	Phase[a]	Crystallinity (±SD%)[b]
1	0	10	7	ZEO-1	76.7 ± 0.002
2	0.05	10	5	Amorphous (ZEO-1)	—
3			7	ZEO-1	61.7 ± 0.026
4	0.1	10	1	Amorphous (ZEO-1)	—
5			3	ZEO-1	95.7 ± 0.001
6	0.15	10	1	Amorphous (ZEO-1)	—
7			3	ZEO-1	97.2 ± 0.025
8	0.2	10	1	Amorphous (ZEO-1)	—
9			2	ZEO-1	88.0
10			3	ZEO-1	100 ± 0.086
11	0.2	5	1	ZEO-1	84.8
12			2	ZEO-1	95.7
13			3	ZEO-1	99.2 ± 0.006
14	0.25	10	7	ZEO-1	79.2 ± 0.018
15	0.3	10	9	ZEO-1	84.3 ± 0.065
16	0.5	10	5	ZEO-1	81.1 ± 0.082
17	0.5	5	30	Amorphous (ZEO-1)	—
18	0.7	10	9	Amorphous	—
19			15	Amorphous	—
20	0[c]	10	18	ZEO-1	90.7
21	0.2[c]	10	3	Amorphous	—
22			5	ZEO-1 (amorphous)	64.3
23			9	ZEO-1	79.2

[a] The product in parentheses is a minor phase. [b] The crystallinity was calculated by comparing the sum of peak areas at 4.05°, 7.04°, 10.78°, 21.70°, and 22.90°. [c] Synthesis at 175 °C.

Table 2 Summary of synthesis results using NH_4F at 190 °C

Entry	F/SiO_2	H_2O/SiO_2	Time (day)	Phase
1	0.1	10	1	Amorphous (ZEO-1)
2			3	ZEO-1
3	0.2	10	1	Amorphous (ZEO-1)
4			5	ZEO-1
5		5	3	Amorphous (ZEO-1)
6			5	ZEO-1
7	0.3	10	3	ZEO-1
8	0.5	10	28	Unknown
9	0.7	10	28	Unknown

SiO_2 ratio of 0.5 (Table 1, entries 16 and 17). At a reduced temperature of 175 °C, it took a longer time, 9 days, to achieve crystalline ZEO-1 zeolites (relative crystallinity 79.2%) compared to its counterpart with the same composition (Table 1, entries 21–23). Fig. S2† compares the variations in crystallinity (%) calculated by the XRD peak area method and the micropore volume method across different F/SiO_2 ratios. The Pearson correlation coefficient ($R \approx 0.8$) indicates a strong positive correlation. No other crystalline impurities were detected in any of the compositions explored, proving the high robustness and reproducibility of the method. The stoichiometrically unbalanced charges of the cation and anion from SDA^+ and F^-, respectively, possibly induce driving forces that facilitate the formation of certain building units of ZEO-1 zeolites, and thus accelerating the crystallization of the ZEO-1 structure, which is further investigated in the following section on crystallization kinetics. Based on these findings, we tentatively designated the synthesis protocol as the "deficient" fluoride synthesis approach.

Considering the toxic and corrosive nature of HF and the difficulty of handling it in industrialization production, NH_4F was explored as an alternative fluoride source for the synthesis of ZEO-1 zeolites. The phases obtained under different synthesis conditions are summarized in Table 2. With the addition of a small amount of NH_4F, the crystallization rate of ZEO-1 zeolites was significantly improved. Specifically, well-crystallized ZEO-1 zeolites were obtained within 3 days of heating at F/SiO_2 ratios of 0.1, 0.2, and 0.3, since all the zeolites possess high micropore volumes measured by Ar adsorption–desorption (Table S1†). By further increasing the F/SiO_2 ratio, only the amorphous phase was obtained even after prolonged heating for up to 28 days (Table 2, entries 8 and 9). In HF medium, the synthesis window is wider, proving the higher efficiency of HF for directing the formation of ZEO-1 zeolites. However, when the synthetic gel system is in an acidic medium, that is, HF or NH_4F is in excessive stoichiometric amounts relative to OSDA, no crystallization of ZEO-1 zeolites is observed.

Collectively, a small amount of fluoride source and an appropriate amount of water, *i.e.*, a lower water content, are proved to be conducive to accelerated crystallization and high reproducibility of ZEO-1 zeolites. This significantly contrasts with most of the previous zeolite syntheses in a fluoride medium, where fluoride was introduced in stoichiometric amounts relative to the positive charge of OSDA or in excess to create an acidic environment.[17,18]

Phase selectivity and morphology

Fig. S3† shows the PXRD patterns of products obtained at different heating times. The PXRD patterns of as-made, calcined, and subsequently NH_4Cl-washed ZEO-1 products obtained at different F/SiO_2 ratios using HF are shown in Fig. 1. It is noted that the phosphorus species originating from the calcination of the as-made zeolites remain trapped in the zeolite channels.[16] All products, as-made (as), calcined (cal), and NH_4Cl-washed (cnw), show characteristic diffraction peaks

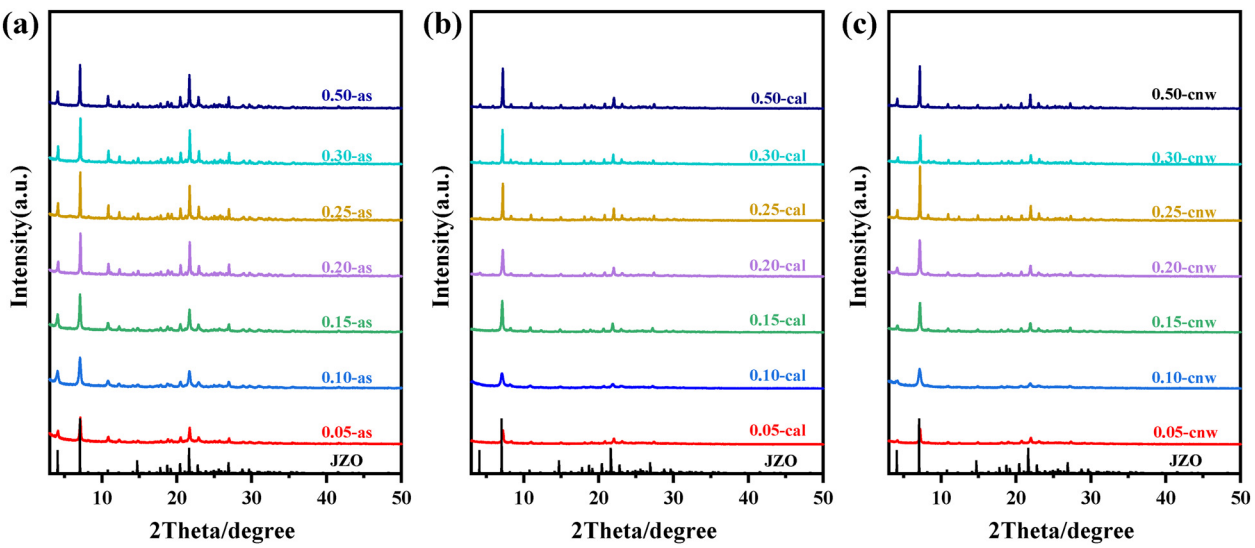

Fig. 1 PXRD patterns of as-made (a), calcined (b) and subsequently NH_4Cl-washed (c) ZEO-1 zeolites obtained with different F/SiO_2 ratios using HF as the fluoride source. The gel molar composition is 1.0 SiO_2 : 0.5 SDAOH : 0.02 Al_2O_3 : x HF : 10 H_2O, x = 0.05–0.7.

consistent with the simulated patterns of ZEO-1 zeolites, with no detectable impurity peaks, confirming that pure ZEO-1 zeolite with good crystallinity was successfully obtained. The ICP results show that the P content of the sample washed with ammonium chloride was 0.07%, much lower than that of the untreated ZEO-1 zeolite (Table S2†). It is noteworthy that a better resolution of diffraction peaks is observed for the NH_4Cl-washed zeolites compared to the calcined counterparts. The PXRD patterns of ZEO-1 zeolites with different F/SiO_2 ratios using NH_4F as a fluoride source are shown in Fig. S4,† which show similar characteristics to those obtained using HF. Although all products retain phase purity, the peak resolution, intensities, and broadness vary depending on the F/SiO_2 ratios and fluoride sources, which is potentially related to the differences in crystallinity and crystal sizes (*vide infra*). It is worth noting that a dense phase, *i.e.*, quartz, formed with prolonged heating (Fig. S5†). The relationship between temperature and crystallization rate was further explored in different media. Fig. S6† shows that higher temperatures accelerated the crystallization rate of the ZEO-1 zeolite, but quartz phases were also observed in OH medium with prolonged heating.

The morphology changes of ZEO-1 zeolites with varying F/SiO_2 ratios were investigated, and the corresponding SEM images are shown Fig. 2. We found that the crystal size of the as-made OH-ZEO-1 obtained here is *ca.* 1 μm (F/SiO_2 = 0), which is larger than that reported in the literature. Upon the addition and increase of HF content, the crystal size gradually increased from *ca.* 50 nm (F/SiO_2 = 0.05) to *ca.* 1.5 μm (F/SiO_2 = 0.3) and then decreased to 200 nm (F/SiO_2 = 0.5). The particle size distribution of ZEO-1 zeolites was further studied, as shown in Fig. S7.† At low F/SiO_2 ratios (*e.g.*, 0.05), the average size of the ZEO-1 crystal was about 61 ± 13 nm, with a narrow error range, while higher F/SiO_2 ratios resulted in broader particle size distributions, *e.g.*, 230 ± 44 nm and 302 ± 32 nm for F/SiO_2 ratios of 0.2 and 0.5, respectively. This suggests that introducing trace fluoride ions promotes uniform nucleation and crystallization due to the formation of a flowable and uniform synthetic gel. In contrast, a further increase in fluoride content produced viscous or powdery synthetic gels that induced non-uniform nucleation and hence crystal growth, finally producing zeolite crystals with a highly non-uniform crystal size distribution. When the F/SiO_2 ratio was increased to 0.3, the average particle size increased to 779 ± 126 nm, with a significantly broader size distribution, indicating that the role of fluoride ions had shifted from promoting nucleation to promoting crystal growth. When the fluorine content was further increased to F/SiO_2 = 0.5, the average particle size decreased back to 230 ± 44 nm, a consequence of dual inhibitory effects from excess fluoride ions: on the one hand, a high fluorine concentration increases gel rigidity, limits monomer diffusion and terminates crystal growth; on the other hand, excess fluoride ions hinder the directional deposition of silicates on the crystal surface by forming stable SiF_6^{2-}. Therefore, the morphology of the product can be flexibly controlled by varying the F content, and hence the alkalinity, of the initial synthetic gel. Despite size variations, all ZEO-1 crystals retain a consistent leaf-like morphology. The crystal morphology of the ZEO-1 zeolites obtained using NH_4F as the fluoride source is shown Fig. S8.† In terms of crystal size, there is no significant variations among samples obtained with the increase of F content. The crystal morphology closely resembled that of ZEO-1 zeolites obtained using HF.

Composition analysis of as-made ZEO-1 zeolites

Elemental analysis (EA) and thermogravimetric analysis (TGA) were performed on as-made ZEO-1 zeolites synthesized with different F/SiO_2 ratios to study their composition and content, as well as the status of the OSDA (Table 3). The Si/Al ratio of ZEO-1 zeolites synthesized using fluoride ranges from approximately 20 to 28, which is much higher than that of ZEO-1 zeolites synthesized in a hydroxide medium (OH-ZEO-1, 12.7). This latter value is comparable with that reported in the literature (12.7 *versus* 14.5).[15] This indicates that adding fluoride

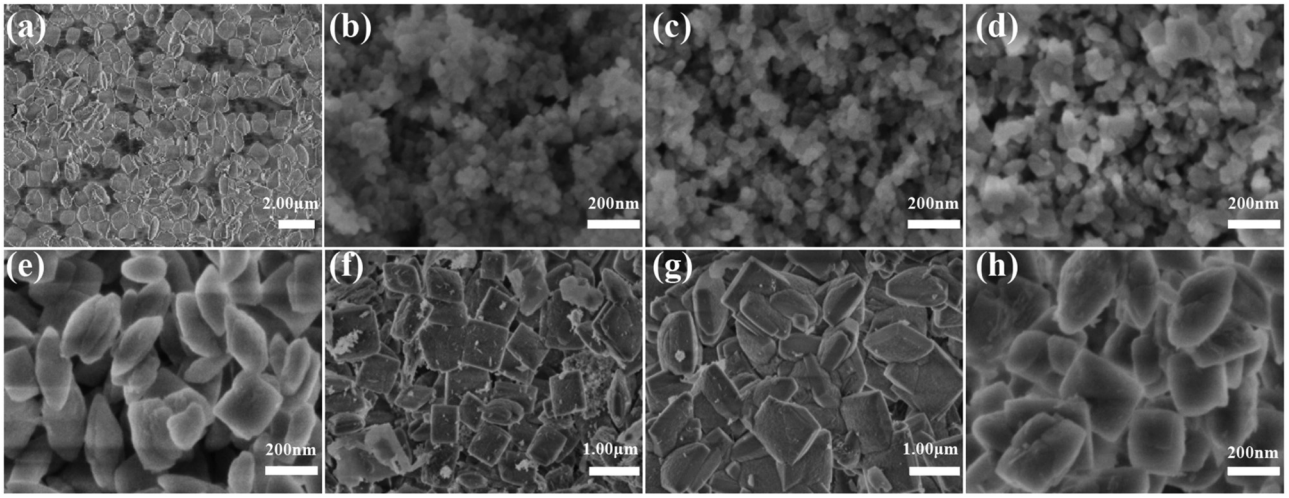

Fig. 2 SEM images of ZEO-1 zeolites obtained with F/SiO_2 ratios of 0 (a), 0.05 (b), 0.10 (c), 0.15 (d), 0.20 (e), 0.25 (f), 0.30 (g) and 0.50 (h) using HF as the fluoride source. The gel molar composition is 1.0 SiO_2 : 0.5 SDAOH : 0.02 Al_2O_3 : *x* HF : 10 H_2O, *x* = 0–0.5.

Table 3 Elemental analysis and composition of as-made ZEO-1 zeolites obtained with different F/SiO_2 ratios

	ICP						CHN			TG weight loss (%)		
Zeolite (F/SiO_2)	Si %	Al %	P %	Si/P	Si/Al	F %	C %	H %	H/C	<200 °C	200–1000 °C	Empirical formula[a]
0	25.97	2.04	2.23	11.62	12.72	—	14.12	2.72	2.33	2.21	15.67	$\|(C_{19}H_{36}P)_{33.7}\|\ [Si_{558.2}Al_{43.9}O_{1248}]$
0.05	31.97	1.17	2.40	13.3	27.25	—	15.91	2.79	2.10	2.37	17.45	$\|(C_{19}H_{36}P)_{37.3}\|\ [Si_{591.4}Al_{21.7}O_{1248}]$
0.1	31.65	1.31	2.15	14.74	24.22	0.39	14.55	2.57	2.12	3.42	15.65	$\|(C_{19}H_{36}P)_{32.4}\|\ [Si_{587.6}Al_{24.2}O_{1248}]$
0.15	31.49	1.36	2.29	13.74	23.18	—	15.43	2.48	1.93	2.54	16.14	$\|(C_{19}H_{36}P)_{35.1}\|\ [Si_{586.1}Al_{25.3}O_{1248}]$
0.2	30.41	1.54	2.67	11.41	19.75	0.32	18.38	2.99	1.95	3.95	16.90	$\|(C_{19}H_{36}P)_{42.9}\|\ [Si_{580.0}Al_{29.4}O_{1248}]$
0.25	29.81	1.27	2.62	11.37	23.53	—	18.23	2.94	1.94	1.73	18.96	$\|(C_{19}H_{36}P)_{41.9}\|\ [Si_{586.6}Al_{24.9}O_{1248}]$
0.3	31.95	1.36	2.51	12.73	23.51	0.57	16.67	2.67	1.92	1.61	18.61	$\|(C_{19}H_{36}P)_{39.5}\|\ [Si_{586.6}Al_{25.0}O_{1248}]$
0.5	30.92	1.33	2.6	11.88	23.24	0.21	18.35	2.91	1.91	1.48	18.90	$\|(C_{19}H_{36}P)_{41.4}\|\ [Si_{586.2}Al_{25.2}O_{1248}]$
0.1[b]	25.80	1.69	2.49	10.34	15.26	0	17.88	3.06	2.05	2.34	17.38	$\|(C_{19}H_{36}P)_{38.9}\|\ [Si_{568.2}Al_{37.2}O_{1248}]$
0.2[b]	27.14	1.47	2.53	10.75	18.45	—	17.71	3.05	2.24	1.79	16.46	$\|(C_{19}H_{36}P)_{39.9}\|\ [Si_{577.1}Al_{31.3}O_{1248}]$
0.3[b]	27.21	1.47	2.30	11.82	18.47	—	16.86	2.90	2.06	1.00	15.95	$\|(C_{19}H_{36}P)_{35.2}\|\ [Si_{577.1}Al_{31.2}O_{1248}]$

[a] The empirical formula was calculated from the ICP results. [b] Synthesis using of NH_4F as the fluoride source.

reduces the aluminum incorporation in the zeolite, which aligns with the previous reports on aluminosilicate zeolites synthesized in F-medium.[19] The explanation is that the fluoride anions interact with aluminum to form AlF_x species (*vide infra*), which, to some extent, hinder the incorporation of Al into the zeolite framework.[20] Notably, ZEO-1 synthesized at F/SiO_2 = 0.2 exhibits a lower Si/Al ratio than other fluoride-containing samples. The H/C ratio of ZEO-1 zeolites synthesized with fluoride matches the theoretical value of 1.89 based on the OSDA, implying that the OSDA is essentially intact, which is further corroborated by the ^{13}C–^{1}H CP NMR spectra (Fig. S9†). Considering the important role of fluoride in the crystallization of ZEO-1, its content was quantified using XRF. The amount of F in the as-made ZEO-1 is negligible, ranging from 0 to 0.57 wt%, indicating that fluoride anions are not encapsulated in the zeolite structure, specifically in the small cavities or cages. The proposed mechanistic role of fluoride in forming zeolite is detailed in the following section. The empirical formula of the as-made ZEO-1 zeolites indicates that the number of OSDA cations per cell is *ca.* 40, which is slightly lower than that of OH-ZEO-1 reported in the literature. All as-made ZEO-1 zeolites synthesized using HF show similar TG curves (Fig. 3) from 25 °C to 1000 °C. At temperatures below 200 °C, the weight loss is due to the desorption of physically adsorbed water. When the temperature rises above 200 °C, a significant weight loss stage occurs up to *ca.* 650 °C, ascribed to the removal of the OSDA from the zeolite channels. Beyond this temperature, the weight loss decreases up to 1000 °C. The weight loss of the OSDA is much lower in F-ZEO-1 (*ca.* 15 wt% to 19 wt%) than in OH-ZEO-1 (23.23 wt%), which can be explained by less Al incorporated into the former, resulting in fewer negative charges that need to be counterbalanced by the OSDA cations. For as-made ZEO-1 synthesized using NH_4F, similar TG weight loss stages were observed (Fig. 3c). Interestingly, the weight loss due to water removal gradually decreased from 1.72 wt% to 1.0 wt% with the increase of NH_4F employed in the synthesis, indicating that the ZEO-1 zeolite becomes more hydrophobic. The Si/Al ratios for these samples are 15.26, 18.45, and 18.47, showing a decreasing trend, which

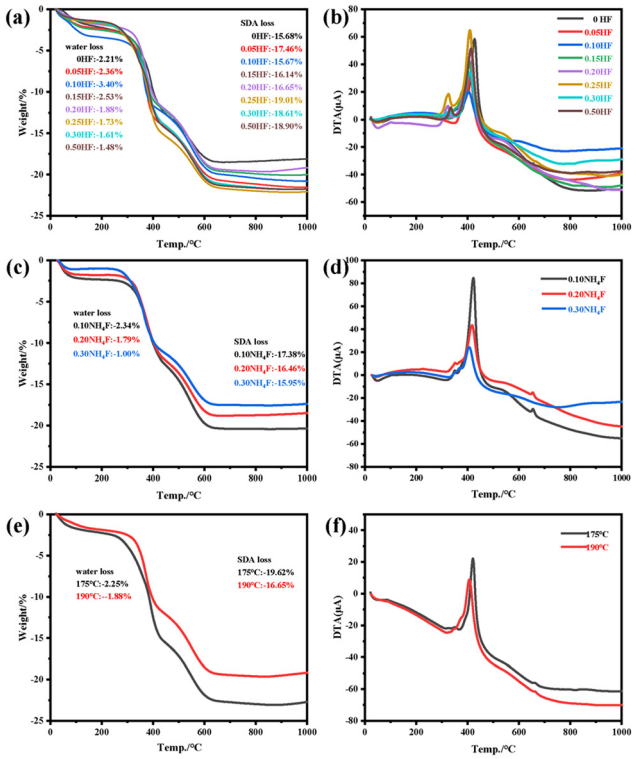

Fig. 3 TG and DTA profiles of ZEO-1 zeolites obtained with different F/SiO_2 ratios using HF (a and b) and NH_4F (c and d) and at different synthesis temperatures (e and f) with a gel molar ratio of 1.0 SiO_2 : 0.5 SDAOH : 0.02 Al_2O_3 : 0.20 HF : 10 H_2O.

is conducive to the decreasing hydrophilicity. The DTA curves show a first endothermic peak between 25 °C and 100 °C, then a weak exothermic peak between 300 °C and 400 °C, followed by an intense exothermic peak between 350 °C and 450 °C, and finally a broad weak exothermic peak at *ca.* 600 °C. The endothermic stage is naturally ascribed to water desorption. The first exothermic stage at 300-400 °C could possibly be assigned to the Hoffman degradation of $TCyMP^+$ cations, while the intense exothermic peak that follows could be assigned to the

decomposition and combustion of $TCyMP^+$ cations balancing framework Al charges. The final stage corresponds to the oxidation of residual species from the previous stage.[19]

Solid-state NMR analysis

^{31}P and ^{13}C MAS solid-state nuclear magnetic resonance (NMR) spectra of as-made ZEO-1 zeolites obtained with an H_2O/SiO_2 of 10 at different F/SiO_2 ratios are shown in Fig. S9,† alongside liquid NMR spectra of the pristine OSDA for comparison. It is observed that the P species in the as-made ZEO-1 zeolites show consistent behavior, with a single resonance peak centered at *ca.* 33 ppm, and the resonances of the C species are also consistent with those of the liquid NMR spectrum of the pristine OSDA, corroborating the intactness of the OSDA cations in the zeolite framework.

The ^{29}Si MAS NMR spectra of as-made ZEO-1 zeolites show that the resonance intensity and resolution increase with rising fluoride content in the synthetic gel (Fig. 4a), indicating enhanced structural ordering of the material. The spectra show 4 distinct resonances centered at *ca.* −100, −105, −110, −116 ppm, which can be largely ascribed to Q^4 species, *i.e.*, Si in fully connected tetrahedral environments.[21] It is worth noting that the resonance at *ca.* −105 ppm might also be assignable to Q^3 [Si(3Si, 1OH)] species due to its overlapping with Q^4 [Si(4Si, 0Al)] species. The resonance between *ca.* −95 and −100 ppm is barely visible, indicating the absence of silanol Q^2 species. After calcination, the resonance intensity at −105 ppm is significantly reduced (Fig. 4b), which may indicate the healing or condensation of Q^3 [Si(3Si, 1OH)] species at the edges of the framework during the calcination process. The broad peaks at *ca.* −116 ppm are almost indistinguishable, which could be due to the slight angular distortion of the ZEO-1 framework.[16] The ^{27}Al MAS NMR spectra of as-made ZEO-1 zeolites show a prominent resonance centered at *ca.* 56 ppm and a shoulder at *ca.* 54 ppm (Fig. 4c), both attributed to tetrahedral aluminum in the framework with two possible crystallographic aluminum species. Resonance signals assignable to extra-framework aluminum species are not detected. The resonance intensity of ZEO-1 obtained with an F/SiO_2 ratio of 0.2 is significantly stronger than that of other ZEO-1 zeolites due to its higher aluminum content, aligning with the elemental analysis results (Table 3). For the calcined ZEO-1 zeolites, the resonance lines of framework aluminum species remain concentrated in the 54–60 ppm region, while resonances in the chemical shift range of 0 to −9 ppm are attributed to the formation of extra-framework aluminum species in monomeric and polymeric compositions (Fig. 4d).[22] Three distinct Al species can be clearly observed in the range of *ca.* 50 to 60 ppm after calcination, centered at *ca.* 51.9, 55.6, and 60.0 ppm, respectively, indicating the presence of at least three different kinds of non-equivalent Al species in the framework.[16] ^{19}F MAS NMR spectra were also collected for as-made ZEO-1 zeolites obtained using F/SiO_2 ratios of 0.1, 0.2 and 0.5 (Fig. S10†). However, the qualitative assignment of the fluoride species is not possible due to the low F content in the samples and the resulting poor spectral resolution.

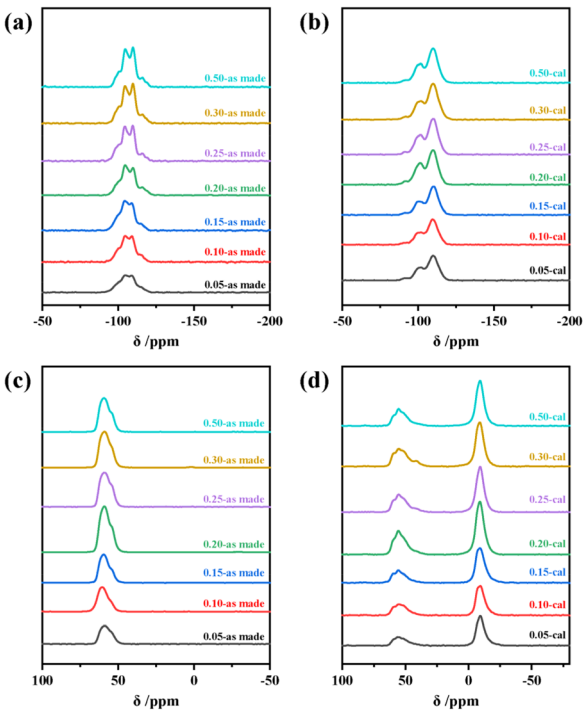

Fig. 4 ^{29}Si (a and b) and ^{27}Al (c and d) MAS NMR spectra of as-made (a and c) and calcined (b and d) ZEO-1 zeolites obtained with a gel molar ratio of 1.0 SiO_2 : 0.5 SDAOH : 0.02 Al_2O_3 : *x* HF : 10 H_2O, *x* = 0–0.5.

Porosity analysis

Fig. 5 shows the physisorption results of P-free ZEO-1 zeolites after calcination and NH_4Cl washing. N_2@77 K and Ar@87 K adsorption–desorption for ZEO-1 zeolites both exhibit type I isotherms (Fig. 5a and b) with similar micropore adsorption volumes, as more explicitly demonstrated by the Ar@87 K isotherms on a logarithmic scale (Fig. 5c). Several samples show

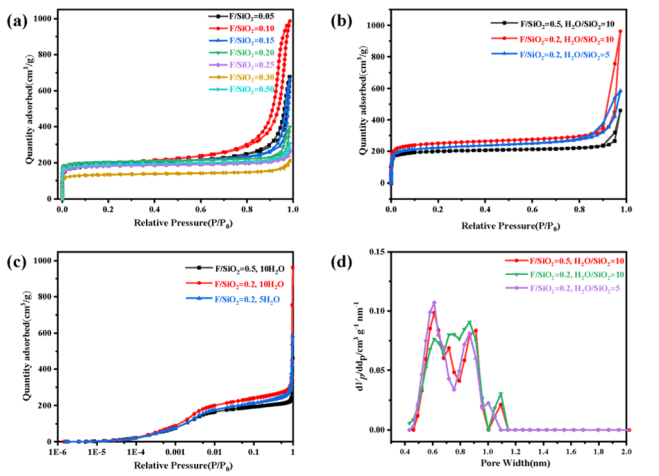

Fig. 5 (a) N_2 adsorption–desorption isotherms, where the gel H_2O/SiO_2 ratio is 10. (b and c) Ar adsorption–desorption isotherms on linear (b) and logarithmic (c) scales and the corresponding (d) pore size distribution calculated using the NLDFT method.

steep uptakes after a P/P_0 of 0.8, indicating the presence of mesopores originating from the pores generated by aggregated crystals or particles. The pore size distribution was calculated using the non-local density functional theory (NLDFT) method based on the Ar physisorption data (Fig. 5d).

The data show three main volumetric adsorptions associated with different pore sizes, centered at *ca.* 0.6 nm, 0.7 nm, and 0.9 nm. The lower values (*ca.* 0.6 and 0.7 nm) are naturally attributed to the size of the 12 MR pore, while the higher value (*ca.* 0.9 nm) is consistent with the maximum opening size of the 16 MR pore. We also investigated ZEO-1 zeolites using NH_4F as a fluoride source. The adsorption and desorption isotherms and the pore size distribution of Ar@87 K are consistent with the above results (Fig. S11†). Based on the Ar physisorption data, the micropore volumes were calculated using the *t*-plot method, as shown in Table S1,† which are important indicators of the zeolite's crystallinity since good PXRD patterns do not necessarily guarantee good crystallinity. The micropore volume obtained from well-crystallized ZEO-1 zeolites ranges between 0.25 and 0.30 $cm^3\ g^{-1}$. Based on our previous work, the ideal micropore volume is *ca.* 0.30 $cm^3\ g^{-1}$ for well-crystallized ZEO-1. It is found that the micropore volume is largest (0.29 $cm^3\ g^{-1}$) for ZEO-1 obtained with a F/SiO_2 ratio of 0.2 and a H_2O/SiO_2 ratio of 10, proving that pure ZEO-1 zeolite with high crystallinity can be facilely and quickly obtained using the deficient fluoride-mediated approach proposed in this study.

Acidity analysis

NH_3-TPD was used to analyse the acidic properties of P-free ZEO-1 zeolites, and the results are shown in Fig. 6. The NH_3-TPD curves show two types of ammonia desorption peaks corresponding to weak and medium-strong acid sites centered at temperature ranges of *ca.* 150–200 °C and 250–400 °C, respectively (Fig. 6a–c). It was found that the ratio of weak and medium-strong acid sites varies in ZEO-1 zeolites obtained with different F/SiO_2 and H_2O/SiO_2 ratios. The amount of NH_3 corresponding to these peaks was calculated from the peak areas and is given in Table S3.† By keeping the F/SiO_2 constant at 0.2, a prominently increased amount of weak acid sites was observed for ZEO-1 obtained at lower water content (H_2O/SiO_2 = 5).

Following the procedures in previous work,[16] di-*tert*-butylpyridine (DTBPy) was employed as an alternative basic probe molecule for infrared spectroscopy studies on the ZEO-1 zeolites obtained *via* the deficient fluoride route. DTBPy can distinguish the Brønsted acid sites at the pore mouths and the surfaces of medium-pore zeolites due to its much larger size than the pyridine molecule. Therefore, the Brønsted acid sites in 3D 12 MR channels and 16 MR channels in ZEO-1 zeolites can be monitored. Fig. S12† shows the infrared spectra of DTBPy probe molecules after diffusion and desorption in ZEO-1 zeolites. The spectral band at 3640 cm^{-1}, characteristic of Brønsted acid sites, is absent, indicating that all Brønsted acid sites of zeolite have interacted with DTBPy. The band at 3370 cm^{-1} corresponds to the stretching vibration of the ≡N–H^+ bond, and this characteristic peak is formed due to complex formation between the Brønsted hydroxyl group and DTBPy.[23] The data demonstrate the full accessibility of the Brønsted acid sites in both the 12-ring and 16-ring channels.

Crystallization kinetics

The crystallization kinetics was studied for gel compositions with a fixed F/SiO_2 ratio of 0.2 at varying H_2O/SiO_2 ratios of 5 and 10, by heating the synthetic gel from 0 h to 72 h (Fig. 7a and b). At a H_2O/SiO_2 ratio of 10, the crystalline phase appeared after heating for 54 h. In contrast, for the composition with a H_2O/SiO_2 ratio of 5, the crystalline phase emerged after only 12 h of heating. Typical S-shaped crystallization curves were obtained based on the relative crystallinity calculated using the PXRD data (Fig. 7c). The crystallization process can be divided into three stages: induction, transition, and crystal growth. The induction period was 36 h with a H_2O/SiO_2 ratio of 10. With a decrease in water content (H_2O/SiO_2 = 5), the induction period drastically shortened to 5 h, indicating that lower water content is conducive to accelerating the crystallization of ZEO-1 zeolites. The nucleation rates ($1/t_{induction}$), calculated using the method reported by Hong *et al.*,[18] were 0.15 and 1.0 for H_2O/SiO_2 ratios of 10 and 5, respectively. For the synthesis with a H_2O/SiO_2 ratio of 5, ZEO-1 zeolites with good crystallinity (90%) were obtained after heating for 30 h. However, the crystallization rate then slowed until a fully-crys-

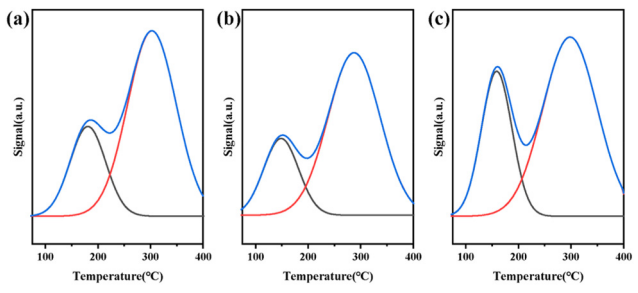

Fig. 6 NH_3-TPD curves of P-free ZEO-1 zeolites. Gel composition: (a) F/SiO_2 = 0.5, H_2O/SiO_2 = 10; (b) F/SiO_2 = 0.2, H_2O/SiO_2 = 10; and (c) F/SiO_2 = 0.2, H_2O/SiO_2 = 5.

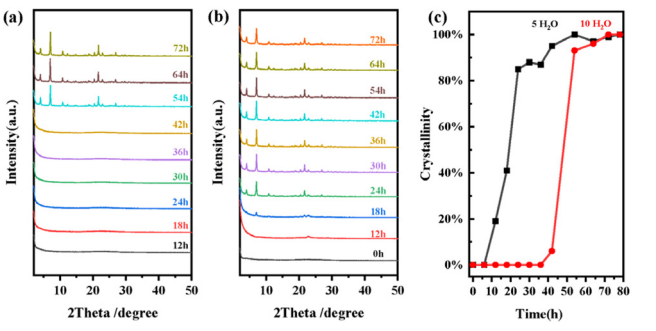

Fig. 7 PXRD patterns of zeolites obtained with H_2O/SiO_2 ratios of 10 (a) and 5 (b) at F/SiO_2 = 0.2. Crystallization kinetics curves of the ZEO-1 zeolite with different water contents at F/SiO_2 = 0.2 (c).

talline product (100% crystallinity) was obtained after 54 h. For the synthesis with a H_2O/SiO_2 ratio of 10, ZEO-1 zeolites with good crystallinity (90%) were achieved after heating for 50 h, which was also evidenced by the almost regular grains shown in Fig. S13.† Then, it took a much faster crystallization rate to obtain fully-crystalline ZEO-1 after heating for another 22 h, in comparison with the synthesis with lower water content. To further quantitatively analyze the crystallization kinetics, the Johnson–Mehl–Avrami–Kolmogorov (JMAK) model[24] was applied to fit the crystallization data collected at 175 °C and 190 °C, as shown in Fig. S14.† The results revealed Avrami rate constants of 1.05×10^{-4} h^{-3} and 2.98×10^{-6} h^{-3} (where n is the Avrami exponent), indicating that increasing temperature significantly accelerates crystallization. The apparent activation energy (E_a), calculated *via* the Arrhenius equation, was determined to be 405.3 kJ mol^{-1}. These findings further corroborate the critical role of fluorine modulation in governing the crystallization kinetics of ZEO-1 zeolites. In short, the deficient fluoride synthesis approach can dramatically shorten the induction period to generate viable nuclei, thus decreasing the crystallization time of the extra-large-pore ZEO-1 zeolite.

To have an in-depth understanding of the role of the deficient fluoride employed in the synthesis, together with a plausible mechanism, comprehensive characterization studies were performed on the products extracted at different heating stages. SEM and TEM images of products obtained with two different water contents at a F/SiO_2 ratio of 0.2 were collected (Fig. 8). For the synthesis with a H_2O/SiO_2 ratio of 5, it can be observed that the product obtained from the as-prepared gel without heating, denoted as the 0 h sample, exhibits amorphous aggregates with irregular morphology (Fig. 8a and d). After prolonged heating for 12 h, particles with elongated layer-like morphology and filamentous features formed, showing a weak and broad X-ray diffraction peak at *ca.* 23° (Fig. 7b). This layered precursor remains stable after calcination upon removing the OSDAs, since several broad diffraction peaks persist (Fig. S15†). Further investigation on this unknown precursor phase is under way. Ill-defined rectangular crystals emerged after further heating to 18 h (Fig. 8b and e), which are attributed to the ZEO-1 phase, as corroborated by the weak characteristic X-ray diffraction peaks alongside those of the precursor (Fig. 7b). The high-magnification TEM image shows crystals with visible lattice fringes attached to the periphery of the layered precursor particles (Fig. 8e, inset), indicating a possible phase transformation during crystallization, *i.e.*, from amorphous to layered precursor and then to crystalline ZEO-1. However, no clear crystallographic registration between the two phases was observed. The phenomenon of phase transformation from a layered precursor to a specific zeolite has been reported previously.[25,26] After heating for 54 h, fully-crystalline ZEO-1 crystals with leaf-like morphology and clear lattice fringes were obtained (Fig. 8f, inset), and the crystal size varies between *ca.* 20 nm and 100 nm. The layered precursor was not detectable in both the microscopy images and PXRD patterns for the synthesis with a H_2O/SiO_2 ratio of 10.

Furthermore, the as-made products obtained at different time intervals were investigated using FTIR spectroscopy (Fig. S16†). Previously, FTIR has been extensively used to investigate the structure and crystallization of zeolites.[27–31] The absorbance band at a wavelength of *ca.* 455 cm^{-1} could

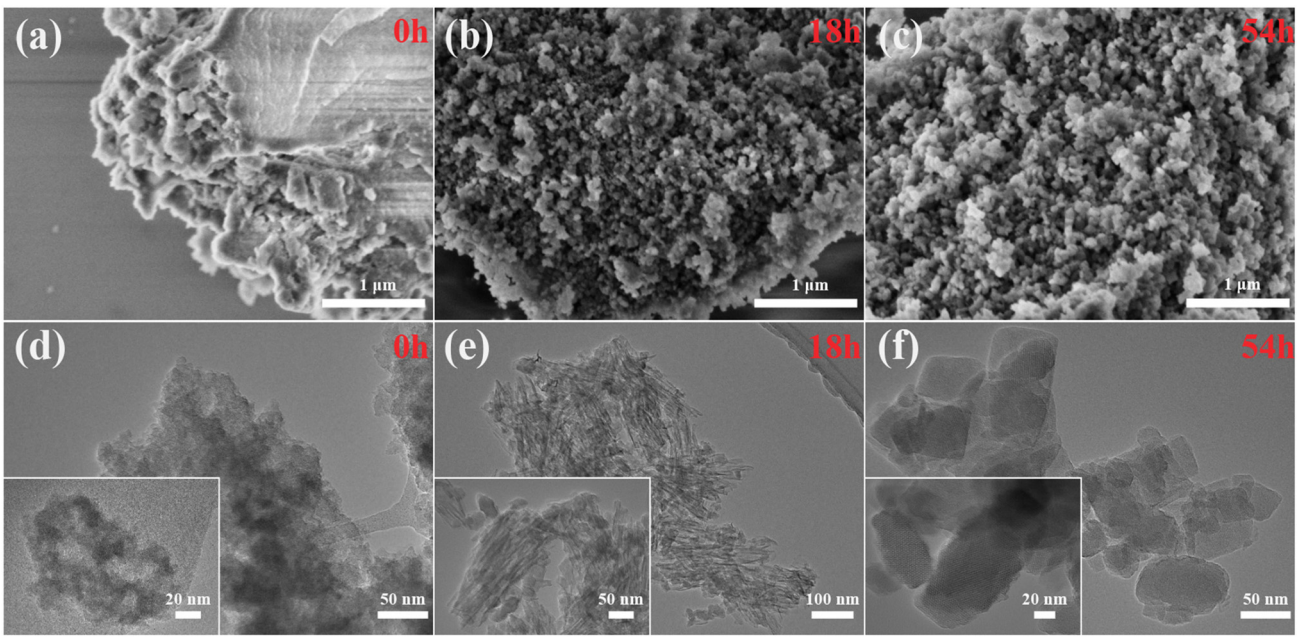

Fig. 8 SEM (a–c) and TEM (d–f) images of as-made products obtained with a H_2O/SiO_2 ratio of 5 and a F/SiO_2 ratio of 0.2 after heating for 0 h (a and d), 18 h (b and e), and 54 h (c and f).

be assigned to the bending vibration of the Si–O bond.[32] The stretching vibration of the Si–O–Si bond corresponds to the wavelength of 1060 cm^{-1}.[33] The peak at 550–600 cm^{-1} corresponds to the stretching vibration of the five-membered ring present in the ZEO-1 zeolite, indicating its atomic order.[34] The 455 cm^{-1} band is very broad during the induction period, and the gradual narrowing of the band with time indicates that the disordered Si–O bonds gradually become ordered. It can be clearly observed in Fig. S16† that the 587 cm^{-1} band is very weak during the induction period and gradually strengthens over time, which again indicates a gradual increase in atomic order and crystallinity consistent with the XRD results.

Solid-state ^{27}Al and ^{29}Si MAS NMR analyses of as-made products obtained at different crystallization times are shown in Fig. 9.

The ^{27}Al MAS NMR spectra show the evolution of Al species over time, from a broad band centered at *ca.* 55 ppm at 0 h to a narrower overlapping band centered at *ca.* 54 ppm with a shoulder at *ca.* 56 ppm at 18 h. With prolonged heating, the band at *ca.* 56 ppm gradually strengthens, while the band at *ca.* 54 ppm weakens, up to a heating time of 72 h. Fig. 9b shows the evolution of different Si species with crystallization time. The resonances of Q^4 (4Si, 0Al) species were not observed at 0 h, and with the extension of crystallization time, the resonance intensity of Q^4 (4Si, 0Al) species gradually increased and became better resolved at 24 h. The intensity and resolution of the resonances did not change significantly after 24 h, indicating that crystallization was nearly completed within 24 h. Fig. 9c shows the evolution of F species with crystallization. A distinct wide peak at −174 to −185 ppm and a relatively weak wide peak at −150 ppm can be clearly observed at 18 h, which are attributed to vibrations of $[AlF_x(H_2O)_{6-x}]^{3-x}$.[35,36] At the initial stage of crystallization, fluorine ions rapidly combine with aluminum species to form complexes. Meanwhile, the F species also combine with the Si species to form SiF_6^{2-}, which corresponds to peak chemical shift values of −122 ppm and −92 ppm. As the crystallization time increases, the −63 ppm peak attributed to fluoride within the t-*mel* cage of the ZEO-1 structure emerges.[37] This observation demonstrates that fluorine species accelerate the formation of t-*mel* cages during zeolite crystallization. The presence of a small amount of fluorine is consequently one of the key factors enabling rapid synthesis of the ZEO-1 zeolite, which is well supported by the experimental data presented in Fig. S10.† The decrease in intensity of the AlF_x species peak may be due to its removal during the zeolite washing process.

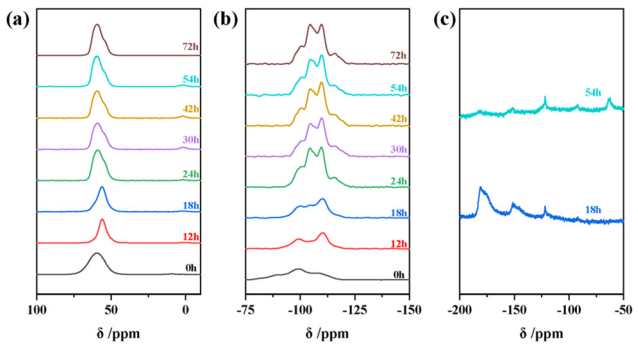

Fig. 9 ^{27}Al (a); ^{29}Si (b) and ^{19}F (c) MAS NMR spectra of as-made products obtained at different crystallization times.

The above results clearly demonstrate that fluoride anions play a significant role in directing the formation of ZEO-1 zeolites. The proposed 'deficient fluoride approach', *i.e.*, the addition of a small portion of fluoride source, is conducive to the earlier formation of primary or secondary building units of the zeolite, hence leading to the formation of viable nuclei to finally realize rapid crystallization of the ZEO-1 zeolite. Despite its important role in the crystallization, the fluoride content is found to be minor in the as-made ZEO-1 zeolites. This leads us to surmise that fluoride anions might act as buffer agents in the synthetic gel, *i.e.*, compensating for partial hydroxide anions and thus lowering the alkalinity of the gel. However, the high viscosity and powdery nature of the synthetic gel and as-made products prevent accurate pH measurement. To prove this hypothesis, we carried out a synthesis using hydrochloric acid instead of HF or NH_4F. The results show that no trace of ZEO-1 could be obtained in the presence of HCl, which also demonstrates that the rapid synthesis of ZEO-1 depends critically on the structure-directing role of fluoride anions rather than merely on the reduction of gel basicity (Fig. S17†).

Catalytic tests

The Friedel–Crafts alkylation reaction, *i.e.*, the alkylation of phenol with *tert*-butanol, was employed to test the catalytic properties of ZEO-1 zeolites. In this reaction, *o*-*tert*-butylphenol (*o*-TBP), *p*-*tert*-butylphenol (*p*-TBP) and 2,4-di-*tert*-butylphenol (DiTBP) are formed as the main products, with a small amount of by-products also produced.[38] The dimensions of the alkylation products, as determined by DFT calculations, are as follows: *o*-TBP (0.57 × 0.68 × 0.43 nm), *p*-TBP (0.79 × 0.43 × 0.38 nm), and 2,4-DTBP (0.79 × 0.68 × 0.43 nm).[39] In the case of zeolite catalysts, the distribution of alkylation products strongly depends on the size and geometry of the micropores where the active sites are located.[38] Consequently, *p*-TBP is the main product formed over Beta zeolites, which possess an interconnected channel system with a cross-section of 0.76 × 0.64 nm. In contrast, *o*-TBP is predominantly formed over Y zeolites. The formation of the bulkier 2,4-DTBP primarily occurs within the supercages of Y zeolite (1.3 nm)[38,39] (an illustration of the proposed reaction mechanism is provided in the ESI, Fig. S18†). Moreover, several studies have demonstrated that phenol conversion is more strongly influenced by the accessibility of acid sites than by their concentration.[40]

Commercial USY (CBV 712, Zeolyst), Beta zeolites (BEA CP814E*, Zeolyst), and ZEO-1 synthesized in the Laboratory of Catalysis and Spectrochemistry (LCS) were used as references for comparative study with ZEO-1 zeolites synthesized using two different H_2O/SiO_2 ratios at a F/SiO_2 ratio 0.2. The results are shown in Fig. 10. All five catalysts show high conversion rates of 82%, 71%, 85%, 84% and 80%, respectively. Both ZEO-1_{LCS} and Beta show high selectivity for *p*-TBP. Beta zeo-

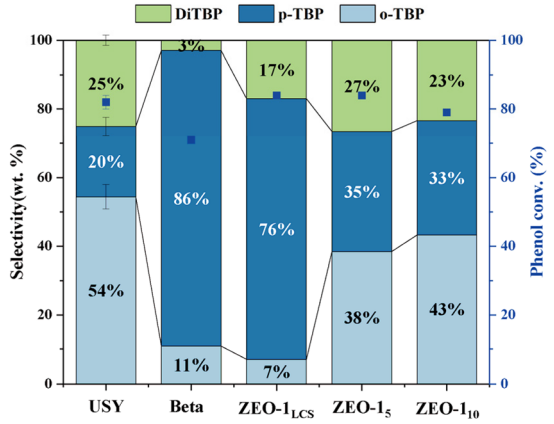

Fig. 10 Product selectivity during phenol alkylation with *tert*-butyl alcohol over ZEO-1, Beta and USY zeolites. ZEO-1_5 and ZEO-1_{10} were synthesized using H_2O/SiO_2 ratios of 5 and 10, respectively, at F/SiO_2 = 0.2.

lite's 12-membered ring channels proved to be structurally favorable for accommodating the linear conformation of *p*-TBP.[38] A previous study attributes ZEO-1's catalytic behavior primarily to its 12 MR supercages due to limited acidic sites in 16 MR channels, resulting in selectivity constraints analogous to those observed in Beta zeolite.[16] Although USY zeolite possesses supercage structures, its spherical pore configuration appears to preferentially facilitate *o*-TBP formation, potentially by restricting the linear conformation of *p*-TBP.

Interestingly, ZEO-1_5 and ZEO-1_{10} exhibit a non-selective product distribution, generating approximately 35% *o*-TBP, 38% *p*-TBP, and 27% DiTBP, a significant deviation from literature reports. This phenomenon may originate from the uniform distribution of acidic sites across both 16-membered and 12-membered ring channels in our ZEO-1 zeolites. Within the 1.1 nm supercage, all three primary products form without restriction, along with trace amounts of by-products such as 2,6-di-*tert*-butylphenol (2,6-DiTBP) and 2,4,6-tri-*tert*-butylphenol (2,4,6-TriTBP) (Table S4†). Furthermore, a comparative evaluation of ZEO-1 synthesized with varying water contents (Fig. 10) reveals marginally enhanced conversion rates (84%) in ZEO-1_5 (the sample synthesized with a low water content). The catalytic results demonstrate that the deficient fluorine synthesis approach used here might have successfully introduced acidic sites into 16 MR channels, simultaneously enhancing selectivity for *o*-TBP and DiTBP while maintaining superior catalytic activity across samples obtained with different synthetic compositions.

Conclusions

A deficient fluoride approach was explored for the successful synthesis of the extra-large-pore aluminosilicate zeolite ZEO-1, achieving a much shorter crystallization time (1 day at 190 °C) and higher reproducibility compared to the reported protocol. With an increase in fluoride amount, the crystal size of the ZEO-1 zeolite initially increases and then decreases, with the largest size reaching 1.5 μm. The as-made ZEO-1 zeolites possess higher Si/Al ratios and lower OSDA loading than their counterparts synthesized in hydroxide medium. Solid-state NMR spectra confirmed both the integrity of the OSDA and partial fluoride retention in the ZEO-1 structure. Crystallization kinetics studies demonstrate that stoichiometrically deficient fluoride anions accelerate nucleation and crystallization rates. The ZEO-1 zeolites synthesized *via* the 'deficient fluoride approach' show catalytic activity for phenol alkylation with *tert*-butyl alcohol comparable to that of ZEO-1_{LCS}, but the products are evenly distributed, suggesting that more Brønsted acid sites might have been successfully introduced in 16 MR channels, hence eliminating size or shape constraints. The deficient fluoride synthesis strategy proposed here opens up the possibility for easier fabrication and wider academic study of ZEO-1.

Author contributions

Peng Lu, Feng Shao and Valentin Valtchev designed and supervised the project. Haijun Yu, Wenjing Zhang, Yiqing Sun, and Doudou Cai collected the data. Haijun Yu and Wenjing Zhang performed the data analysis and interpreted the results. Nourrdine Chaouati, Ludovic Pinard, and Mohammad Fahda tested the catalytic performance. Haijun Yu, Wenjing Zhang, Peng Lu, and Feng Shao drafted the manuscript. Feng Shao, Peng Lu and Valentin Valtchev obtained funding. All authors contributed to the revision of the manuscript and approved the final version to be published. Guangying Fu participated in revising the manuscript. All authors agree to be accountable for all aspects of the work, ensuring that questions related to the accuracy or integrity of any part of the work are appropriately investigated and resolved.

Data availability

The data that support the findings of this study are available on request from the corresponding authors.

Conflicts of interest

There are no conflicts to declare.

Acknowledgements

The ZeoMat Group acknowledges the starting grant provided by the Qingdao Institute of Bioenergy and Bioprocess Technology and the support from the Shandong Energy Institute (SEI S202107). P. L. acknowledges the support from the Qingdao New Energy Shandong Laboratory of International Cooperation Project (QNESL ICP 202305). V. V.

and P. L. acknowledge the collaboration within the Sino-French International Research Network 'Zeolites' framework. The authors are indebted to Yida Zhou and Shutao Xu from Dalian Institute of Chemical Physics for collecting the ^{19}F NMR data.

References

1 M. E. Davis, Ordered porous materials for emerging applications, *Nature*, 2002, **417**, 813–821.
2 A. Corma, Inorganic Solid Acids and Their Use in Acid-Catalyzed Hydrocarbon Reactions, *Chem. Rev.*, 1995, **95**, 559–614.
3 P. Lu, S. Ghosh, M. Dorneles de Mello, H. S. Kamaluddin, X. Li, G. Kumar, X. Duan, M. Abeykoon, J. A. Boscoboinik, L. Qi, H. Dai, T. Luo, S. Al-Thabaiti, K. Narasimharao, Z. Khan, J. D. Rimer, A. T. Bell, P. Dauenhauer, K. A. Mkhoyan and M. Tsapatsis, Few-Unit-Cell MFI Zeolite Synthesized using a Simple Di-quaternary Ammonium Structure-Directing Agent, *Angew. Chem., Int. Ed.*, 2021, **60**, 19214–19221.
4 H. Dai, Y. Shen, T. Yang, C. Lee, D. Fu, A. Agarwal, T. T. Le, M. Tsapatsis, J. C. Palmer, B. M. Weckhuysen, P. J. Dauenhauer, X. Zou and J. D. Rimer, Finned zeolite catalysts, *Nat. Mater.*, 2020, **19**, 1074–1080.
5 M. E. Davis, C. Saldarriaga, C. Montes, J. Garces and C. Crowdert, A molecular sieve with eighteen-membered rings, *Nature*, 1988, **331**, 698–699.
6 M. Estermann, L. B. McCusker, C. Baerlocher, A. Merrouche and H. Kessler, A synthetic gallophosphate molecular sieve with a 20-tetrahedral-atom pore opening, *Nature*, 1991, **352**, 320–323.
7 A. Corma, M. J. Díaz-Cabañas, F. Rey, S. Nicolopoulus and K. Boulahya, ITQ-15: The first ultralarge pore zeolite with a bi-directional pore system formed by intersecting 14- and 12-ring channels, and its catalytic implications, *Chem. Commun.*, 2004, 1356–1357, DOI: 10.1039/B406572G.
8 A. Corma, M. J. Díaz-Cabañas, J. L. Jordá, C. Martínez and M. Moliner, High-throughput synthesis and catalytic properties of a molecular sieve with 18- and 10-member rings, *Nature*, 2006, **443**, 842–845.
9 J. Sun, C. Bonneau, Á. Cantín, A. Corma, M. J. Díaz-Cabañas, M. Moliner, D. Zhang, M. Li and X. Zou, The ITQ-37 mesoporous chiral zeolite, *Nature*, 2009, **458**, 1154–1157.
10 A. Corma, M. J. Díaz-Cabañas, J. Jiang, M. Afeworki, D. L. Dorset, S. L. Soled and K. G. Strohmaier, Extra-large pore zeolite (ITQ-40) with the lowest framework density containing double four- and double three-rings, *Proc. Natl. Acad. Sci. U. S. A.*, 2010, **107**, 13997–14002.
11 J. Jiang, J. L. Jorda, M. J. Diaz-Cabanas, J. Yu and A. Corma, The Synthesis of an Extra-Large-Pore Zeolite with Double Three-Ring Building Units and a Low Framework Density, *Angew. Chem., Int. Ed.*, 2010, **49**, 4986–4988.
12 J. Jiang, J. L. Jorda, J. Yu, L. A. Baumes, E. Mugnaioli, M. J. Diaz-Cabanas, U. Kolb and A. Corma, Synthesis and Structure Determination of the Hierarchical Meso-Microporous Zeolite ITQ-43, *Science*, 2011, **333**, 1131–1134.
13 J. Jiang, Y. Yun, X. Zou, J. L. Jorda and A. Corma, ITQ-54: a multi-dimensional extra-large pore zeolite with 20 × 14 × 12-ring channels, *Chem. Sci.*, 2015, **6**, 480–485.
14 E. Kapaca, J. Jiang, J. Cho, J. L. Jordá, M. J. Díaz-Cabañas, X. Zou, A. Corma and T. Willhammar, Synthesis and Structure of a 22 × 12 × 12 Extra-Large Pore Zeolite ITQ-56 Determined by 3D Electron Diffraction, *J. Am. Chem. Soc.*, 2021, **143**, 8713–8719.
15 Q.-F. Lin, Z. R. Gao, C. Lin, S. Zhang, J. Chen, Z. Li, X. Liu, W. Fan, J. Li, X. Chen, M. A. Camblor and F.-J. Chen, A stable aluminosilicate zeolite with intersecting three-dimensional extra-large pores, *Science*, 2021, **374**, 1605–1608.
16 M. Fahda, J. Fayek, E. Dib, H. Cruchade, N. Pichot, N. Chaouati, L. Pinard, P. S. Petkov, G. N. Vayssilov, A. Mayoral, B. Witulski, L. Lakiss and V. Valtchev, Investigating the Physicochemical Properties of an Extra-large Pore Aluminosilicate ZEO-1, *Chem. Mater.*, 2024, **36**, 5405–5421.
17 D. Shi, K.-G. Haw, C. Kouvatas, L. Tang, Y. Zhang, Q. Fang, S. Qiu and V. Valtchev, Expanding the Synthesis Field of High-Silica Zeolites, *Angew. Chem., Int. Ed.*, 2020, **59**, 19576–19581.
18 J. Bae and S. B. Hong, Zeolite synthesis by the excess fluoride approach in the presence of piperidinium-based structure-directing agents, *Microporous Mesoporous Mater.*, 2021, **327**, 111422.
19 M. A. Camblor, A. Corma and S. Valencia, Synthesis in fluoride media and characterisation of aluminosilicate zeolite beta, *J. Mater. Chem.*, 1998, **8**, 2137–2145.
20 B. Louis and L. Kiwi-Minsker, Synthesis of ZSM-5 zeolite in fluoride media: an innovative approach to tailor both crystal size and acidity, *Microporous Mesoporous Mater.*, 2004, **74**, 171–178.
21 E. Lippmaa, M. Maegi, A. Samoson, M. Tarmak and G. Engelhardt, Investigation of the structure of zeolites by solid-state high-resolution silicon-29 NMR spectroscopy, *J. Am. Chem. Soc.*, 1981, **103**, 4992–4996.
22 T. Liu, X. Li, J. Shim, O. J. Curnow, J. Choi and A. C. K. Yip, Accelerated Crystallization Kinetics of MFI Zeolite via Imidazolium-Based Synthesis, *Cryst. Growth Des.*, 2024, **24**, 4122–4130.
23 K. Góra-Marek, K. Tarach and M. Choi, 2,6-Di-tert-butylpyridine Sorption Approach to Quantify the External Acidity in Hierarchical Zeolites, *J. Phys. Chem. C*, 2014, **118**, 12266–12274.
24 M. Fanfoni and M. Tomellini, The Johnson-Mehl- Avrami-Kohnogorov model: A brief review, *Nuovo Cimento D*, 1998, **20**, 1171–1182.
25 M. A. Camblor, A. Corma, M.-J. Díaz-Cabañas and C. Baerlocher, Synthesis and Structural Characterization of MWW Type Zeolite ITQ-1, the Pure Silica Analog of MCM-22 and SSZ-25, *J. Phys. Chem. B*, 1998, **102**, 44–51.
26 A. Rojas and M. A. Camblor, HPM-2, the Layered Precursor to Zeolite MTF, *Chem. Mater.*, 2014, **26**, 1161–1169.

27 D. Lesthaeghe, P. Vansteenkiste, T. Verstraelen, A. Ghysels, C. E. A. Kirschhock, J. A. Martens, V. V. Speybroeck and M. Waroquier, MFI Fingerprint: How Pentasil-Induced IR Bands Shift during Zeolite Nanogrowth, *J. Phys. Chem. C*, 2008, **112**, 9186–9191.
28 H. Geng, G. Li, D. Liu and C. Liu, Rapid and efficient synthesis of CHA-type zeolite by interzeolite conversion of LTA-type zeolite in the presence of N, N, N-trimethyladamantammonium hydroxide, *J. Solid State Chem.*, 2018, **265**, 193–199.
29 T. Zorigt, C. Zhai, J. Jiao, J. Sun and X. Wu, Synthesis and Characterizations of High Crystallized Clinoptilolite by Structure Directing Agent Method and its Crystallization Kinetics, *ChemistrySelect*, 2021, **6**, 2855–2861.
30 S. L. Burkett and M. E. Davis, Mechanisms of Structure Direction in the Synthesis of Pure-Silica Zeolites. 1. Synthesis of TPA/Si-ZSM-5, *Chem. Mater.*, 1995, **7**, 920–928.
31 S. Park, H. Onozuka, S. Tsutsuminai, J. N. Kondo and T. Yokoi, Insight into the crystallization mechanism of the CON-type zeolite, *Microporous Mesoporous Mater.*, 2020, **302**, 110213.
32 S. K. Hoffmann, J. Goslar, S. Lijewski, I. Olejniczak, A. Jankowska, A. Werbińska and S. Kowalak, Sulfur Pigments Synthesized from Zeolite LTA under Vacuum and in Air. XRD and Spectroscopic (UV–vis, FTIR, Raman, ESR, ESE) Characterization, *Ind. Eng. Chem. Res.*, 2010, **49**, 8192–8199.
33 G. Huang, P. Ji, H. Xu, J.-G. Jiang, L. Chen and P. Wu, Fast synthesis of hierarchical Beta zeolites with uniform nanocrystals from layered silicate precursor, *Microporous Mesoporous Mater.*, 2017, **248**, 30–39.
34 A. Aerts, C. E. A. Kirschhock and J. A. Martens, Methods for in situ spectroscopic probing of the synthesis of a zeolite, *Chem. Soc. Rev.*, 2010, **39**, 4626–4642.
35 P. Caullet, L. Delmotte, A. C. Faust and J. L. Guth, Synthesis of LEV-type zeolite from aqueous nonalkaline fluoride aluminosilicate gels, *Zeolites*, 1995, **15**, 139–147.
36 L. Delmotte, M. Soulard, F. Guth, A. Seive, A. Lopez and J. L. Guth, 19F MAS n.m.r. studies of crystalline microporous solids synthesized in the fluoride medium, *Zeolites*, 1990, **10**, 778–783.
37 J. Martinez-Ortigosa, R. Millán, J. Simancas, J. A. Vidal-Moya, C. Martineau-Corcos, F. Rey and T. Blasco, New insights into fluoride's role in MFI zeolites: unveiling the link between location and synthesis conditions, *Inorg. Chem. Front.*, 2025, **12**, 2359–2367.
38 E. Dumitriu and V. Hulea, Effects of channel structures and acid properties of large-pore zeolites in the liquid-phase tert-butylation of phenol, *J. Catal.*, 2003, **218**, 249–257.
39 L. Desmurs, C. Cammarano, G. Ramona, R. Gaumard, T. Mineva, A. Sachse, J.-D. Comparot, T. Cacciaguerra, D. Cot, O. Gimello, A. Galarneau and V. Hulea, Finding the Compromise between Brønsted Acidity and Mesoporosity in Hierarchical ZSM-5 Zeolites, *ChemCatChem*, 2023, **15**, e202300167.
40 J. Li, L.-L. Lou, Y. Yang, H. Hao and S. Liu, Alkylation of phenol with tert-butyl alcohol over dealuminated HMCM-68 zeolites, *Microporous Mesoporous Mater.*, 2015, **207**, 27–32.

